

# Topology of the Pore-Region of a K<sup>+</sup> Channel Revealed by the NMR-Derived Structures of Scorpion Toxins

Jayashree Aiyar,\* Jane M. Withka,† James P. Rizzi,‡ David H. Singleton,‡ Glenn C. Andrews,‡ Wen Lin,‡ James Boyd,‡ Douglas C. Hanson,‡ Mariella Simon,\* Brent Dethlefs,\* Chao-lin Lee,\* James E. Hall,\* George A. Gutman,† K. George Chandy\*

\*Department of Physiology and Biophysics  
University of California  
Irvine, California 92717

†Department of Microbiology and Molecular Genetics  
University of California  
Irvine, California 92717

‡Pfizer Central Research  
Groton, Connecticut 06340

## Summary

**The architecture of the pore-region of a voltage-gated K<sup>+</sup> channel, Kv1.3, was probed using four high affinity scorpion toxins as molecular calipers. We established the structural relatedness of these toxins by solving the structures of kaliotoxin and margatoxin and comparing them with the published structure of charybdotoxin; a homology model of noxiustoxin was then developed. Complementary mutagenesis of Kv1.3 and these toxins, combined with electrostatic compliance and thermodynamic mutant cycle analyses, allowed us to identify multiple toxin-channel interactions. Our analyses reveal the existence of a shallow vestibule at the external entrance to the pore. This vestibule is ~28–32 Å wide at its outer margin, ~28–34 Å wide at its base, and ~4–8 Å deep. The pore is 9–14 Å wide at its external entrance and tapers to a width of 4–5 Å at a depth of ~5–7 Å from the vestibule. This structural information should directly aid in developing topological models of the pores of related ion channels and facilitate therapeutic drug design.**

## Introduction

Voltage-gated potassium (K<sup>+</sup>) channels regulate diverse biological processes (Chandy and Gutman, 1995). The P-region, a short stretch of amino acids located between the fifth and sixth transmembrane segments, is the primary determinant of ion selectivity and is also the target for many K<sup>+</sup> channel blockers. Delineation of the spatial organization of the residues in the P-region would help define the structure of the pore and be valuable for understanding the mechanisms of ion permeation.

Scorpion toxins block K<sup>+</sup> channels with 1:1 stoichiometry (MacKinnon and Miller, 1988) and have previously been used as molecular probes to map residues in the P-region of the *Shaker* channel (Goldstein et al., 1994; Stocker and Miller, 1994; Hidalgo and MacKinnon, 1995). Extensive mutagenesis of charybdotoxin (ChTX) revealed that residues clustered on the “undersurface” of the toxin are criti-

cal for binding to the channel pore (Goldstein et al., 1994). Subsequent studies using a complementary mutagenesis strategy, coupled with quantitative methods such as electrostatic compliance (Stocker and Miller, 1994) and thermodynamic mutant cycle analysis (Hidalgo and MacKinnon, 1995), revealed single or dual pairs of interacting toxin-channel residues.

A detailed topological map of the P-region could be obtained by a process of triangulation if multiple toxin-channel pairs were defined. To achieve this goal, we studied a mammalian channel, Kv1.3, which is blocked at high-affinity by four related scorpion toxins. This channel regulates the membrane potential in T-lymphocytes (Lewis and Cahalan, 1995), and Kv1.3 blockers, including scorpion toxins, suppress T-cell activation (DeCoursey et al., 1984; Price et al., 1989; Leonard et al., 1992; Lin et al., 1993). To use these toxins as molecular calipers, we solved the structures of kaliotoxin (KTX) and margatoxin (MgTX), created a homology model of noxiustoxin (NTX), and used the published structure of ChTX (Bontems, et al. 1992). Using these toxins as structural templates and applying quantitative methods to determine the spatial proximity of particular toxin and channel residues, we were able to define the geometry of a shallow vestibule at the external entrance to the pore. This information places substantial spatial constraints on any model of the P-region of voltage-gated K<sup>+</sup> channels.

## Results

### Use of Multiple Toxins as Molecular Probes of the Channel Vestibule

The sequence of the P-region and flanking regions of the Kv1.3 channel is shown in Figure 1A. In earlier studies, we demonstrated that ChTX, KTX, MgTX, and NTX are potent blockers of Kv1.3 (Grissmer et al., 1990, 1994). These four toxins contain 37–39 amino acids and share three disulfide bonds (Figure 1B) that constrain backbone movement, thereby minimizing structural perturbations upon binding to the channel. Flexibility of the side chains may, however, contribute some degrees of freedom to toxin-channel interaction. A fundamental assumption underlying our studies is that the four toxins bind to Kv1.3 with a similar geometry, an assumption supported by their high degree of similarity in sequence (Figure 1B) and tertiary folds (discussed below).

Many P-region residues in Kv1.3 were mutated and examined for their effect on block by toxins (Table 1). Three residues were chosen for more detailed study (H404, D386, G380), since mutations at these positions altered Kv1.3's sensitivity to the toxins (Table 1). Our approach was to identify channel mutants that differentially affected block by the four toxins, then, by comparing the toxin structures, to identify unique residues that might be responsible for these differences. Complementary mutagenesis of the identified toxin residue (Goldstein et al., 1994), coupled

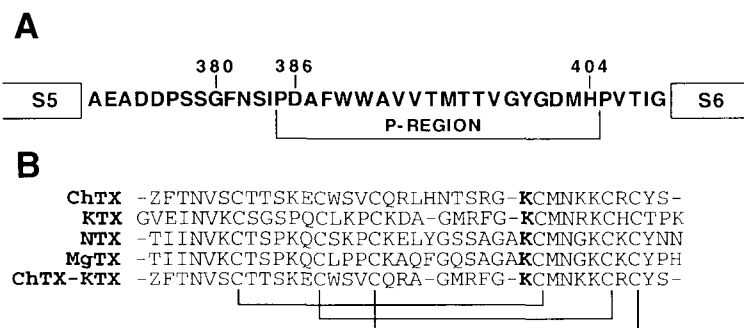


Figure 1. Amino Acid Sequences of the Kv1.3 P-Region and of a Family of Scorpion Toxins (A) The P-region and flanking sequences of Kv1.3. (B) Amino acid alignment of toxins. The three internal disulfide bonds are indicated by brackets. K27 in ChTX and KTX corresponds to K28 in MgTX and NTX.

with electrostatic compliance (Stocker and Miller, 1994) and mutant cycle analyses (Hidalgo and MacKinnon, 1995), served to confirm specific predicted interactions and yielded estimates of the distance between the interacting residues.

The tertiary structures of ChTX (Bontems et al., 1992) and MgTX (Johnson et al., 1994) have been determined by nuclear magnetic resonance (NMR); since the atomic coordinates of MgTX have not been released from the Protein Data Base, we had to independently determine its structure for the purpose of using it as a molecular template. When these experiments were initiated, the structures of KTX and NTX remained to be determined; we therefore solved the structure of KTX and developed a homology model of NTX based on the closely related MgTX.

**Solution Structure of KTX**

The secondary structure of KTX was obtained by short- and medium-range nuclear Overhauser effects (NOEs; Figure 2A) and by <sup>3</sup>J(HN-H $\alpha$ ) coupling constants. Two

strands of the antiparallel  $\beta$  sheet contain residues F25-C28 (strand 2) and C33-T36 (strand 3) with a reverse turn at residues M29-K32 (Figure 2B). A third  $\beta$  strand at the N-terminus consists of residues V2-C8 (strand 1). Residues V2-I4 make standard  $\beta$ -sheet contacts with H34-C35 followed by a  $\beta$  bulge involving residues N5 and V6. Standard antiparallel  $\beta$ -sheet NOEs are observed for K7 and C8 with K32. An  $\alpha$  helix that connects  $\beta$  strands 1 and 2 involves residues P12-A21.

Figure 3A shows a final ensemble of 15 tertiary structures of KTX in which there is an average of 1.3 violations over 0.05 Å and no individual violation over 0.076 Å. The average root-mean-square deviation between members of the ensemble and the average structure including all residues is 0.46 Å for backbone atoms and 1.09 Å for all heavy atoms.

The tertiary structure of KTX (Figure 3A) contains a three-stranded anti-parallel  $\beta$  sheet with the  $\alpha$  helix lying across strands 2 and 3. This orientation is restrained by two disulfide bonds involving residues C14 and C18 in the

Table 1. Block of Wild-Type and Mutant Kv1.3 by Scorpion Toxins

Channel	ChTx (nM)	KTX (nM)	MgTX (nM)	NTX (nM)	ChTX-KTX (nM)
Kv1.3	0.71 ± .19	0.41 ± 0.23	0.06 ± .02	0.31 ± .12	0.77 ± 0.15
H404A	0.64 ± .47	0.50 ± .10	ND	0.12	
H404T	0.46 ± .38	0.77 ± .63	0.10 ± 0.05	0.20 ± 0.02	
H404V	0.18 ± .13	1.05 ± .34	ND	0.60	
H404L	9.1 ± 1.3	13 ± 2.4	ND	ND	
H404R	>1000	>1000	>1000	>100	
H404Y	1.2 ± 0.68	0.06 ± 0.03	0.08 ± 0.01	0.24 ± 0.10	0.08 ± .01
D386N	2.3 ± .88	40 ± 20	0.87 ± 0.30	0.53 ± 0.05	22 ± 12
D386E	0.74 ± .40	1.9 ± .59	0.05 ± 0.01	0.35 ± 0.15	2.6 ± .79
D386K	260 ± 82	950 ± 100	3.5 ± .75	5.5 ± 2.1	1000 ± 14
G380T	11 ± 0.42	3.1 ± 0.35	0.30 ± 0.10	0.5 ± 0.30	
G380E	11 ± 6	300 ± 65	0.15 ± 0.06	0.7 ± 0.33	
G380V	600 ± 150	130 ± 30	1.1 ± 0.55	1.3 ± 0.60	
G380Q	>1000	>1000	1.1 ± 0.30	1.1 ± 0.50	
G380H	>1000	>1000	12 ± 11	5.7 ± 2.4	
G380L	820 ± 152	470 ± 26	2.5 ± 0.7	0.87 ± 0.01	
G380F	>1000	>1000	>1000	>1000	
S379A	1.0 ± 0.16	ND	ND	ND	
N382K	3.4 ± 1.2	1.3 ± 0.40	0.20 ± 0.12	ND	
S383N	5.3 ± 0.19	3.7 ± 1.3	ND	1.1	

Numbers represent K<sub>0.5</sub> for channel block (nM) ± SD; n = 2-10, except for those values with no SD; ND = not done. Deletion of the first four residues of KTX has little effect on KTX potency: (KTX [3-38]: 0.68 ± 0.45 nM; KTX [5-38]: 0.18 ± 0.10 nM); deletion of the last two residues results in a decrease in potency of ~ 10-fold (KTX [1-36]: 3.5 ± 2.0 nM). In contrast, deletion of the last three residues of MgTX has a substantial effect on channel block (MgTX [1-36] > 100 nM), and replacing these with the corresponding residues from KTX does not restore potency (MgTX [37-39/TPK]: 38 nM).

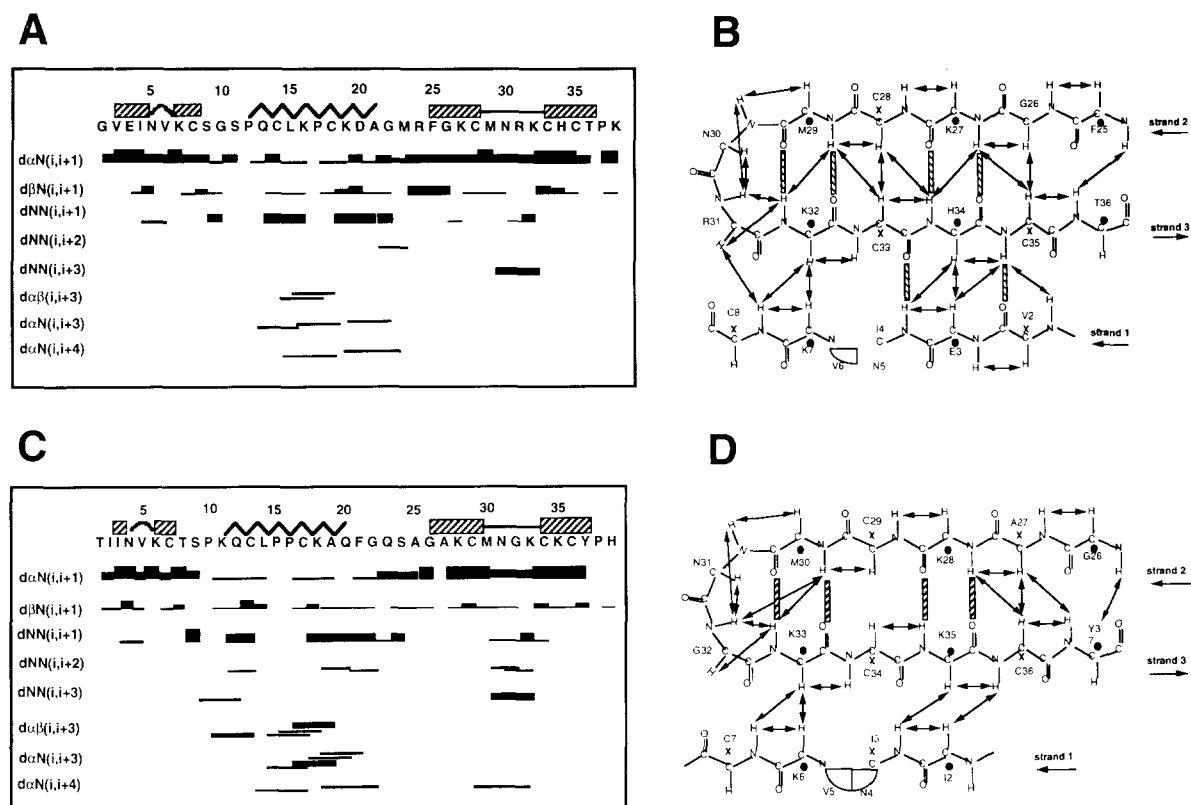


Figure 2. Determination of Solution Structures of KTX and MgTX by NMR

(A) Bar graph showing short- and medium-range NOEs used to generate KTX structures. Strong, medium, and weak NOEs are represented by thick, medium, and thin lines, respectively. Secondary structure is indicated on top, with  $\beta$  strands represented as rectangles and the  $\alpha$  helix as a zigzag line.

(B) Schematic showing (as double-headed arrows)  $\beta$ -sheet NOEs for KTX that are observed for strands 1, 2, and 3. The H-bonds included in the calculations, based on standard  $\beta$ -sheet NOEs, are shown as broken lines. Side chains oriented toward the solvent/channel are indicated by filled circles, and those oriented toward the helix are indicated with an X.

(C) Bar graph showing all the relevant NOE spectroscopy data used to generate MgTX structures (see A).

(D) Schematic showing  $\beta$ -sheet NOEs for MgTX (see B). The NOEs involving C29 and C34 could not be unambiguously determined, owing to degeneracy of the chemical shifts of their  $H\alpha$  protons at several temperatures and pH levels.

helix with C33 and C35, respectively, in strand 3 of the  $\beta$  sheet. The loop including residues G22–M23–R24 connects the  $\alpha$  helix to strand 2. The putative sites of interaction for the toxin and the channel involve many of the solvent-exposed side chains of the  $\beta$  sheet residues that are oriented opposite to those contacting the helix as well as the loop residue R24. In the calculated structures, the reverse turn between strands 2 and 3, involving residues M29–K32, can assume two conformations: a Type II and a nonideal Type I turn. A value of 6.6 Hz was obtained for the  $^3J(HN-H\alpha)$  coupling constant for residue 3 (R31) of the turn. This coupling constant is not indicative of either a true Type I or Type II turn (Wüthrich, 1986) and may indicate conformational averaging in solution (Johnson et al., 1994).

The tertiary fold of KTX is identical to those of homologous scorpion toxins including ChTX (Bontems et al., 1992), iberiotoxin (Johnson et al., 1992), MgTX (Johnson et al., 1994), and agitoxin 2 (AgTX2; Krezel et al., 1995). However, a significantly altered tertiary fold has recently been reported for a truncated KTX molecule (Fernandez et al., 1994). Although we have no satisfactory explanation

for this difference, the absence of the C-terminal lysine and differences in sample pH and ionic strength might contribute to these conflicting structures.

#### Solution Structure of MgTX

The secondary structure of MgTX is similar to that of KTX and has been determined by the NOEs shown in Figure 2C and by  $^3J(HN-H\alpha)$  coupling constraints. A three-stranded antiparallel  $\beta$  sheet involving residues G26–C29 (strand 2) and C34–Y37 (strand 3) is connected by a Type I reverse turn formed by residues M30–K33 (see Figure 2D). Although strand 1 at the N-terminus is less well defined in MgTX than in KTX, several standard NOEs are observed for I2–I3 to K35–C36. A similar  $\beta$  bulge is observed for residues N4 and V5 followed by standard NOEs for K6 and C7 to K33 (see Figure 2D). The  $\beta$  bulge observed in strand 1 at the N-terminus in MgTX and KTX has also been observed in AgTX2 (Krezel et al., 1995). An  $\alpha$  helix is formed for residues K11–Q20 and includes a P–P sequence at positions 15 and 16.

A final ensemble of 14 tertiary structures of MgTX shown in Figure 3B is of similar quality to that of KTX, with an average of 2.2 violations over 0.05 Å and no individual

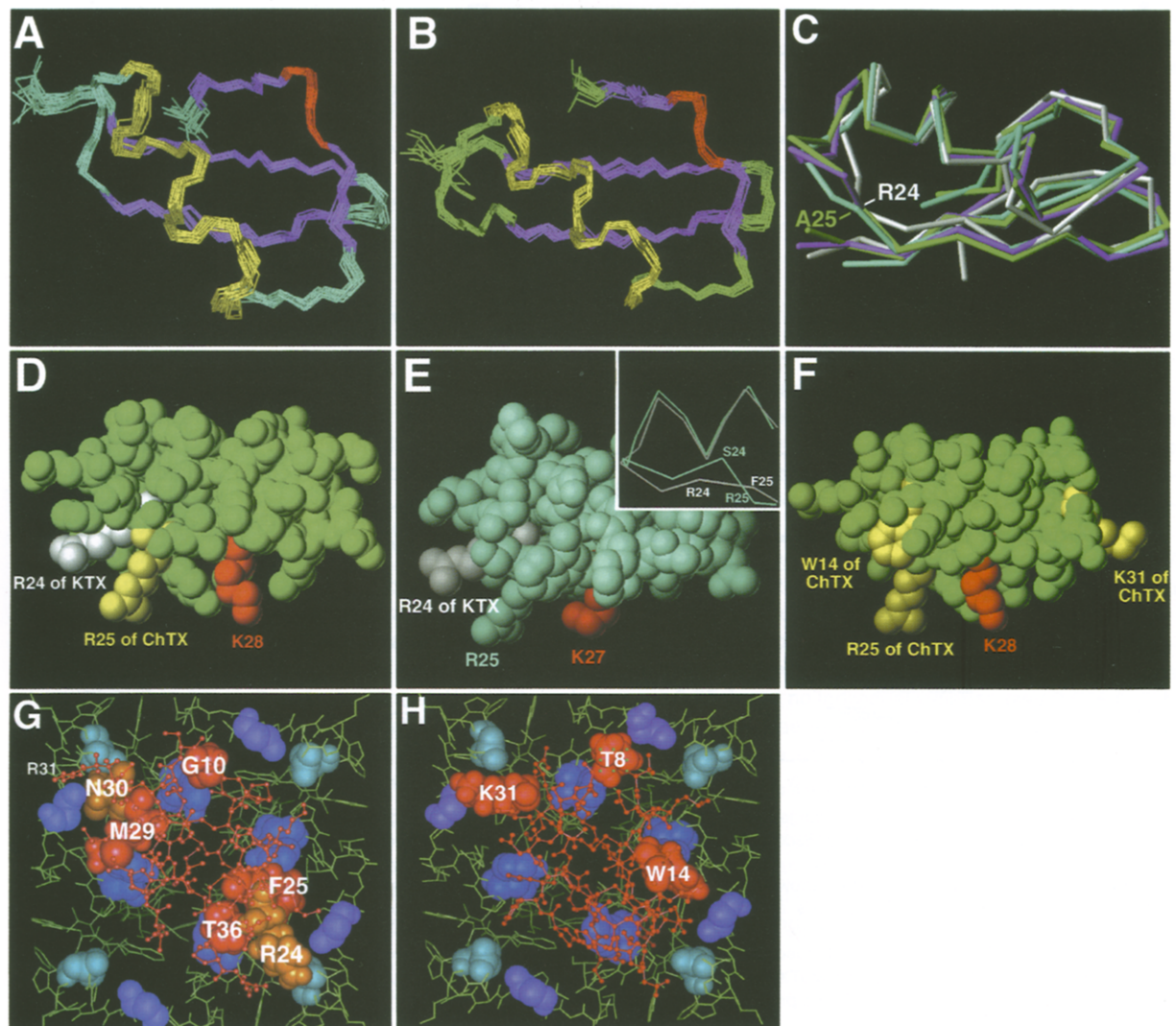


Figure 3. Backbone and Space-Filling Representations of Scorpion Toxins, and Docking of KTX and ChTX into the Kv1.3 Channel Model

(A) Superposition of backbone atoms of all residues for 15 structures of KTX. The secondary structure is represented in blue for loop regions, magenta for  $\beta$  strands, red for the  $\beta$  bulge and yellow for the  $\alpha$  helix.  
 (B) Superposition of backbone atoms of all residues for 14 structures of MgTX. The secondary structure is represented in green for loop regions, magenta for  $\beta$  strands, red for the  $\beta$  bulge, and yellow for the  $\alpha$  helix.  
 (C) Overlap of the backbones of NMR structures of ChTX (blue), KTX (white), and MgTX (green), and that of a homology model of NTX (magenta). Residues KTX-R24 and MgTX-A25, positioned very close to each other, are indicated (see text).  
 (D) Side view of space-filling MgTX structure (green). Residue K28 (corresponding to ChTX-K27) is shown in red. ChTX-R25 is superimposed in yellow and KTX-R24 in white.  
 (E) Side view of space-filling structure of ChTX (blue). Residue K27 is shown in red, and KTX-R24 is superimposed in white. Inset, stick diagram comparing the loops linking the  $\alpha$  helix and  $\beta$  sheet in ChTX and KTX. ChTX (blue) shows residues 15–26; KTX (white) depicts residues 16–26 and is one residue shorter and shaped differently. Residues at positions 24 and 25 are labeled.  
 (F) Side view of space-filling structure of MgTX (green), with K28 shown in red. Bulky residues of ChTX (W14, R25, K31) are superimposed in yellow.  
 (G and H) Models (top views) of KTX (G) and ChTX (H) docked within the Kv1.3 vestibule. Most channel residues are indicated as green stick figures; shown in space-filling representation are channel residues H404 (dark blue), D386 (light blue), and G380 (lavender). The toxins are shown as red ball-and-stick models, except for certain residues displayed in space-filling mode (see below). (G) KTX. Toxin residues G10, M29, F25, and T36 are positioned close to each of the four H404's (dark blue) in the Kv1.3 homotetramer, and KTX residues R24 and N30 close to opposite D386s (pale blue); R31 (red ball-and-stick, top left) is also in the vicinity of D386. (H) ChTX. T8, W14 and K31 are positioned close to three of the four G380s (lavender) in the homotetramer.

violation over 0.092 Å. The root-mean-square deviation for each member of the ensemble and the average structure is 0.52 Å for backbone atoms and 0.96 Å for all heavy atoms. The tertiary fold of MgTX (Figure 3B) is identical to the structure reported by Johnson et al. (1994) and very similar

to that of KTX (Figure 3A), except in the loop connecting the  $\alpha$  helix to strand 2 of the  $\beta$  sheet (see below).

#### Comparison of Toxin Structures

An overlap of the NMR-derived backbone structures of KTX, MgTX, and ChTX illustrates the close similarity

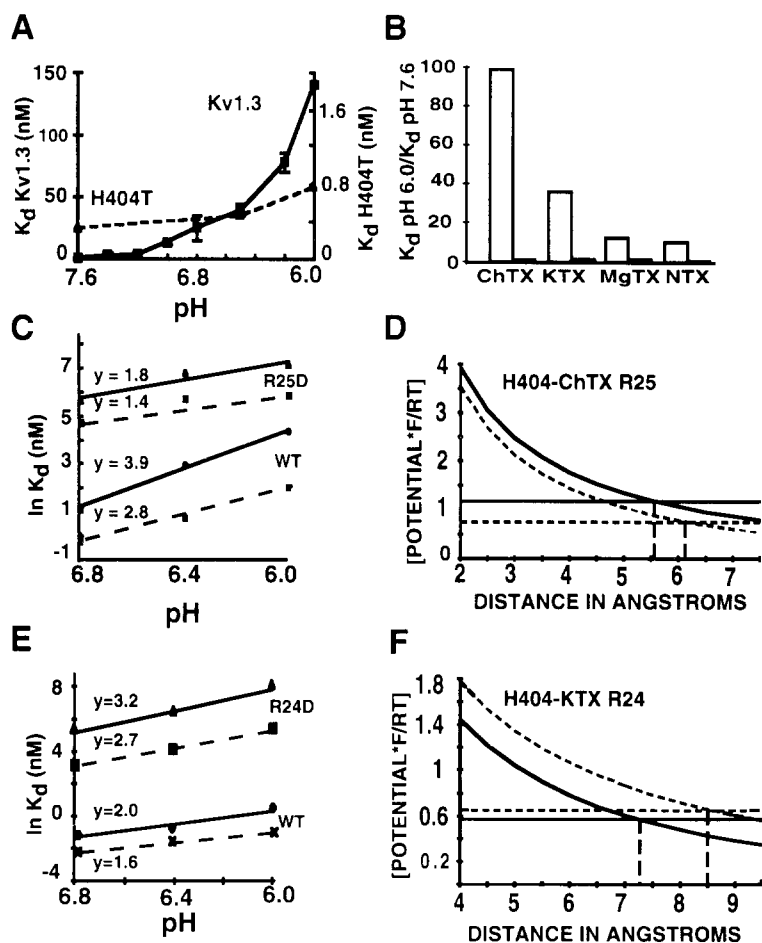


Figure 4. Electrostatic Interaction between Kv1.3-H404 and Toxin Residues ChTX-R25 and KTX-R24

(A) pH-dependence of ChTX block of Kv1.3 (solid line) and H404T mutant (dashed line). Note that the scales for Kv1.3 and H404T are markedly different, reflecting the increased sensitivity of the mutant channel to ChTX block (see Table 1).

(B) Comparison of pH dependence on block of WT Kv1.3 and H404T by ChTX, KTX, MgTX, and NTX. Open bars, WT Kv1.3 (H404); solid bars, H404T. Values for H404T at pH 7.6 are given in Table 1. At pH 6.0 the values are ChTX =  $0.67 \pm 0.23$  nM; KTX =  $0.44 \pm 0.12$  nM; MgTX =  $0.03 \pm 0.01$  nM; NTX =  $0.23 \pm 0.1$  nM ( $n = 3-4$ ).

(C) Effect of change in ionic strength and pH on block by ChTX and ChTX-R25D. Least square slopes at 25 mM (dashed lines) and 100 mM (solid lines) ionic strength.

(D) Charge-pair separation ( $\text{\AA}$ ) versus electrostatic compliance for ChTX-R25:H404. Horizontal lines, experimentally derived values; curved lines, theoretical values. Solid lines, 100 mM; dashed lines, 25 mM.

(E) Effect of change in ionic strength and pH on block by KTX and KTX-R24D.

(F) Charge-pair separation ( $\text{\AA}$ ) versus electrostatic compliance for +KTX-R24:H404 (see D for details).

among their tertiary folds (Figure 3C). This similarity, together with the high degree of sequence identity between NTX and MgTX, strongly suggests that NTX also shares a similar tertiary fold, as seen in the homology model of NTX (based on MgTX; see Figure 3C and Experimental Procedures).

The difference between MgTX and KTX noted above (Figure 3C) can be seen on the left side of this superposition, by comparing the loop region of KTX (white) with that of MgTX (green). This loop connecting the  $\alpha$  helix to strand 2 of the  $\beta$  sheet is extended by two residues in MgTX (F21-G22-Q23-S24-A25). It is relatively well defined and oriented toward the helix, as determined by NOEs between K18 and residues G22, Q23, and A25. The homologous loop in KTX consists of residues G22-M23-R24, with R24 of KTX in a position similar to A25 of MgTX.

#### H404 in Kv1.3 is 2.4-6 $\text{\AA}$ from Residue 25 in ChTX and KTX, and 5.3-8.5 $\text{\AA}$ from R24 in KTX

Histidine 404, based on the model of Guy and Durrell (1994), is positioned at the outer entrance to the channel pore. Protonation of H404 might therefore electrostatically repel any positively charged toxin residues in its vicinity. We tested this possibility by examining the pH-dependence of toxin block (Figures 4A and 4B). A change in pH from 7.6 to 6.0 diminished Kv1.3's sensitivity to block by

ChTX  $\sim 100$ -fold, by KTX  $\sim 40$ -fold, and by MgTX and NTX by only  $\sim 10$ -fold. Replacement of H404 with threonine abolished the pH-dependent effect on block by all four toxins (Figures 4A and 4B), indicating that H404 is most likely the only titratable residue, in either the channel or these toxins, that affects toxin block. The enhanced pH-sensitivity of ChTX, relative to MgTX and NTX, could be explained by electrostatic repulsion by protonated H404 of a positively charged residue that is present on the undersurface of ChTX but not MgTX or NTX. Pairwise comparisons of the NMR-derived structures of these toxins revealed ChTX-R25 as the only candidate residue; Figure 3D shows a superposition of ChTX-R25 on the MgTX structure.

An estimate of the distance between R25 and H404 was obtained by a generalization of the electrostatic compliance method of Stocker and Miller, 1994 (see equations 1 and 2 in Experimental Procedures). As the pH is varied from 6.8 to 6.0, the  $K_d$  of channel block by ChTX and ChTX-R25D decreases, but the least square slopes are not appreciably different at 25 mM versus 100 mM ionic strength (Figure 4C). Such behavior would be expected if R25 and H404 sense each other electrostatically and are within one Debye length of each other. Figure 4D plots the charge-pair separation in angstroms ( $r_{ij}$  in equation 1) versus the electrostatic compliance,  $\sigma(i,j)$ . The experi-

mental (horizontal lines) and theoretical (curves; calculated from equation 1) compliance curves intersect at  $r_{ij}$  values of  $\sim 5.5\text{--}6.0$  Å.

Thermodynamic mutant cycle analysis (Hidalgo and MacKinnon, 1995) was used (see equations 3–5 in Experimental Procedures) as an independent tool to gauge the distance between R25 and H404. The  $\Omega$  value for the pair ChTX-R25D:Kv1.3 [pH 6.8 to pH 6.0] is 11, corresponding to a coupling energy of  $5.9 \times 10^3$  joules per mole and an R25:H404 separation of  $\sim 2.5$  Å. Thus, both quantitative methods indicate that ChTX-R25 lies in close proximity (2.4–6 Å) to H404.

#### **KTX-R24 is 5.3–8.5 Å from H404**

Protonation of H404 reduced KTX potency, but to a lesser extent than ChTX (Figure 4B). This could be explained by the presence of a positively charged residue on the undersurface of KTX, absent in NTX and MgTX, which is in the vicinity of H404, but not as close as R25 in ChTX. Comparison of the NMR structures of KTX and MgTX points to R24 as the only unique basic residue in this region (see Figure 3D).

Protonation of H404 was associated with a reduction in the  $K_d$  for KTX and the KTX-R24D mutant, but the slopes were similar at 25 mM and 100 mM ionic strengths (Figure 4E), suggesting that R24 and H404 interact electrostatically and are close together. The experimental  $\sigma(i,j)$  values determined from the data in Figure 4E intersect the theoretical compliance values with  $r_{ij}$  in the range of 7–8.5 Å (Figure 4F). This estimate agrees with mutant cycle analyses that places the two residues  $\sim 5.3$  Å apart (= 2.5 and coupling energy of  $2 \times 10^3$  joules per mole for the pair KTX-R24D:Kv1.3 [pH 6.8 to pH 6.0]).

#### **H404 in Kv1.3 Is Close to F25 in KTX**

A comparison of the backbone structures of ChTX and KTX shows that R25 in ChTX and F25 in KTX are both positioned at the beginning of the  $\beta$  sheet and are very close in the overlapped structures (see Figure 3E, inset). If R25 in ChTX is  $\sim 2.4\text{--}6$  Å from H404, as the protonation data suggest, then F25 in KTX must also be in the vicinity of this channel residue. KTX might therefore be expected to block Kv1.3 more potently if an aromatic residue were placed at position 404 in the channel (e.g., H404Y), owing to an aromatic–aromatic interaction. Such short range interactions between aromatic residues are known to occur in the hydrophobic core of many proteins, to have typical coupling energies of 1–2 kcal per mole, and to be the result of quadrupole electrostatics and hydrophobic packing that decrease as  $1/r^5$  (Burley and Petsko, 1985, 1989). Such an interaction should not be seen if H404 were replaced with a nonaromatic residue, nor would the H404Y substitution be expected to enhance the channel's sensitivity to ChTX, which has a nonaromatic residue (R25) at the homologous position. Consistent with our expectation, Kv1.3's sensitivity to KTX is enhanced  $\sim 7$ -fold by the H404Y mutation, while the five other nonaromatic substitutions at this position either decrease or do not alter potency (see Table 1). Also as predicted, the H404Y mutation did not appreciably alter block by ChTX, but increased  $\sim 10$ -fold the sensitivity to a ChTX–KTX chimera (see Figure 1B)

containing residues 21–25 (AGMRF) from KTX in place of the corresponding ChTX loop (see Table 1); this result can be explained by an aromatic–aromatic interaction between Kv1.3-H404Y and F25 in the chimera. Collectively, these results support the conclusion that F25 in KTX, like R25 in ChTX, is positioned close to H404 in Kv1.3.

#### **D386 in Kv1.3 Interacts with R24 in KTX**

Neutralization of D386 (D386N) caused a 100-fold reduction in the sensitivity of Kv1.3 to inhibition by KTX, but had little effect on ChTX or NTX (Figure 5A; see Table 1). This dramatic change in potency is consistent with the presence of a positively charged residue on the undersurface of KTX, but not ChTX, which is located near D386. Comparison of the NMR structures of ChTX and KTX reveals R24 as the only positively charged residue unique to KTX in this region (see Figure 3E). This residue is located in the loop connecting the  $\alpha$  helix and  $\beta$  sheet in the toxin, which is one residue shorter and has a different shape than the corresponding region in ChTX (see Figure 3E, inset). If R24 in KTX interacts with D386, then introduction of arginine at the homologous position in ChTX should enable this toxin to interact with D386. Due to the known structural differences in the loop region of KTX and ChTX, point mutations could not be used to demonstrate the R24:D386 interaction. We therefore replaced the entire six-residue loop in ChTX with the five-residue loop (AGMRF) from KTX (see Figure 1B), in the expectation of conferring on ChTX the ability to interact with D386. As seen in Figure 5A, the ChTX–KTX loop chimera behaves very much like KTX. Since R24 is the only positively charged residue in the transferred loop, these data are consistent with the existence of an interaction between KTX-R24 and D386 in Kv1.3.

#### **D386 and R24 Interact Electrostatically and Are within 3–4 Å of Each Other**

As the charge at position 386 is changed from negative to positive (D→N→K), the blocking affinity of KTX and the KTX-R24D mutant decreases, but the least square slopes are remarkably similar at 25 and 100 mM ionic strengths (Figure 5B). This indicates that R24 and D386 participate in a close range electrostatic interaction. An estimate of the distance between R24 and D386 was obtained by electrostatic compliance. Figure 5C plots the charge–pair separation in Å versus  $\sigma(i,j)$ ; the experimental (horizontal lines) and theoretical (curved lines) compliance values intersect at  $r_{ij}$  values of 3.5–4.0 Å. Thermodynamic mutant cycle analysis gave similar results. An value of 1287 was obtained for the pair D386K:R24D, corresponding to a coupling energy of  $17 \times 10^3$  joules and a charge–pair separation of 3.5 Å. Collectively, data from both quantitative methods strongly suggest that D386 interacts intimately with KTX-R24.

Replacement of D386 with the longer glutamate (the E side chain is  $\sim 2$  Å longer than D when measured from  $C_\alpha$  to the terminal oxygen) might be expected to hinder the formation of a salt bridge and render the channel less sensitive to KTX, but not to ChTX. Consistent with this expectation, the D386E mutation showed a small but re-

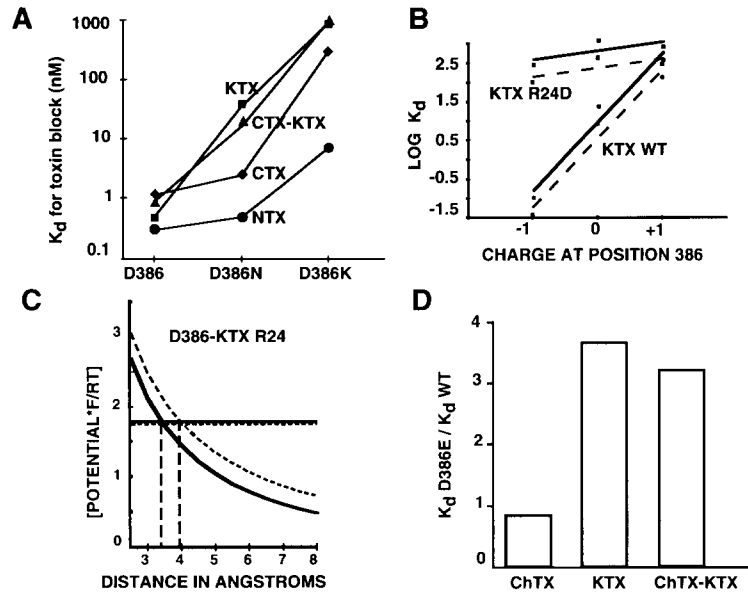


Figure 5. Electrostatic Interaction between Kv1.3-D386 and KTX-R24

(A) Effect of charge at channel position 386 on block by KTX, ChTX, NTX, and ChTX-KTX. (B) Effect of ionic strength on block by KTX and KTX R24D of D386 mutants. Least square slopes are shown at 25 mM (dashed lines) and 100 mM (solid lines) ionic strength. (C) Charge-pair separation (Å) versus electrostatic compliance. Horizontal lines, experimentally derived values; curved lines, theoretical values. Solid lines, 100 mM; dashed lines, 25 mM. (D) Effect of D386E mutation on block by KTX, ChTX, and ChTX-KTX.

producibly reduction (3.5-fold) in the channel's sensitivity to block by KTX and the ChTX-KTX loop mutant (which contains R24), but had no effect on block by ChTX (Figure 5D). A similar reduction in toxin block of *Shaker* was observed with the homologous D431E mutation (MacKinnon et al., 1990).

In summary, KTX-R24 is 3–4 Å from the N-terminal end of the P-region (D386) and slightly more distant (5.3–8 Å) from the C-terminal end (H404). KTX-F25 and ChTX-R25, residues positioned close to H404 (3–6 Å), might therefore be expected to lie about 6–8 Å from D386.

#### ChTX-R25 Is in the Vicinity of D386

Although the D386N mutation had only a small effect on ChTX potency, replacing this residue with positively charged lysine (D386K) resulted in a channel with ~350-fold lower ChTX sensitivity (Figure 5A). This result could be explained by the presence of a unique basic residue in ChTX that does not interact directly with D386, but is sufficiently close to be electrostatically repelled by a lysine at that channel position. R25, the only unique positive charge on the undersurface of ChTX, lies about 6–8 Å from D386 (discussed in previous paragraph) and would be close enough to be repelled by D386K, but would not be affected by the D386N mutation.

#### G380 Is Close to W14 and K31 in ChTX, and L15 and R31 in KTX

The *Shaker* model of Guy and Durrell (1994) has G380 lying at the outer margin of the external vestibule. Based on a single mutation of the homologous residue in *Shaker*, F425G, Goldstein et al. (1994) suggested that ChTX block of this channel might depend on the size of the amino acid at this position. To test this prediction, we examined the effect of eight residues at position 380 in Kv1.3 on toxin block.

Kv1.3's sensitivity to toxin block progressively de-

creased as the size of the residue at position 380 increased (Figure 6). This sensitivity was appreciably greater for ChTX and KTX relative to NTX and MgTX (Figure 6). A size change from 60 to 138 Å<sup>3</sup> (G380E) rendered the channel resistant to KTX, whereas a change to 144 Å<sup>3</sup> (G380V) made it insensitive to ChTX. A more substantial increase in size (G380F, 190 Å<sup>3</sup>) was needed to confer resistance to MgTX and NTX. This result suggests that a relevant dimension in KTX and ChTX is larger (perhaps owing to the presence of bulky residues) than in the other two toxins. We searched for such bulky residues by pairwise comparisons of the structures of ChTX and KTX versus MgTX and NTX. As shown in the comparison of ChTX and MgTX structures (see Figure 3F), three bulky residues (W14, R25, and K31) are present in ChTX but not in MgTX, and the distance between the farthest residues (positions 14 and 31) is greater in ChTX than in MgTX (Figure 6, legend). Similar comparisons identified KTX positions L15 and R31 as possible bulky residues that may contribute to the larger dimension of KTX over MgTX and NTX (Figure 6, legend). Shrinking this dimension in ChTX and KTX, by replacement of the bulky residues with the corresponding smaller residues of NTX, might reduce the size dependence of their block and shift the curve to the right.

As seen in the inset in Figure 6, double mutants of both ChTX-(W14S + K31G) and KTX-(L15S + R31G) were markedly less affected by size changes at position 380 than the wild-type (WT) toxins; a size change from G to E diminished sensitivity to KTX-(L15S + R31G) only 30-fold while changing the K<sub>d</sub> for WT KTX ~600-fold. Similarly, a size change from G to Q caused only a 15-fold change in K<sub>d</sub> for the "shrunk" mutant ChTX-(W14S + K31G), while the channel's sensitivity to WT ChTX decreased ~1000-fold. These results support the idea that residues 14/15 and 31/32 are each close to opposing G380 residues in the channel tetramer.

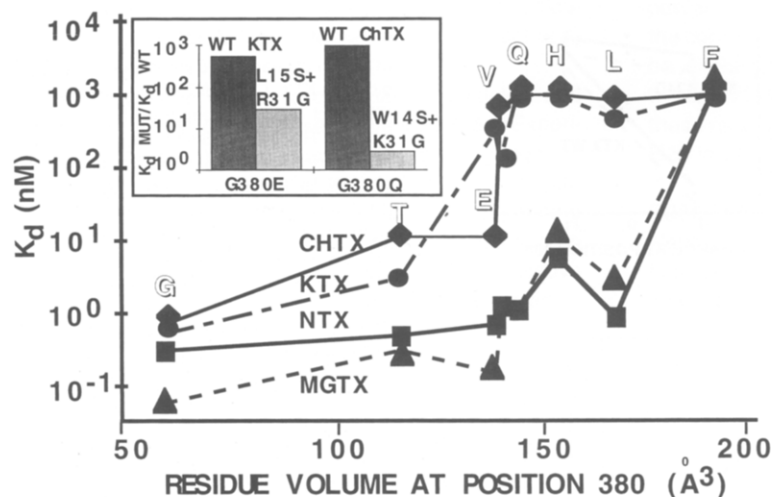


Figure 6. Relationship between the Size of the Residue at Kv1.3 Position 380 and Toxin Block. The relevant dimension lies between residues 14 and 31 in ChTX (25–27 Å), 15 and 31 in KTX (21–26 Å), 14 and 32 in MgTX (20–22 Å), and 14 and 32 in NTX (19–20 Å). We used the average of the longest and shortest distances between the heavy atoms of these residues. Inset, comparison of block of WT and mutant (G380E, G380Q) Kv1.3 channels by KTX, KTX L15S + R31G, ChTX, and ChTX W14S + K31G.

### Substitutions at Position 27 in KTX: Interactions with the Channel Pore

Lysine 27, a residue conserved in all scorpion toxins, is critical for blockade of the *Shaker* and calcium-activated “maxi” K<sup>+</sup> channels and is thought to interact with a residue in the pore (Park and Miller, 1992; Goldstein and Miller, 1993; Stampe et al., 1994). To study this interaction further, we made several substitutions at position 27 in KTX and determined their effects on blocking affinities.

#### Neutralization of K27 Reduces Toxin Potency

Replacement of K27 with asparagine or with the nonnatural neutral amino acid norleucine (which resembles lysine but lacks the terminal amine) reduced toxin potency 300-fold (Table 2). This demonstrates the importance of the terminal amine at position 27 and suggests that this residue may interact directly or through space with negatively charged residues in the pore (e.g., the cluster of four D402s).

#### Replacement of K27 with Positively Charged Residues of Varying Length and Bulk

Replacement of K27 with nonnatural lysine analogues of varying lengths made little or no change in toxin potency (Table 2), indicating that their terminal amino groups, extending 2.2–7.9 Å from C<sub>α</sub>, are all suitably positioned to interact with the target residue(s) in the pore. One possible explanation for this result is that the terminal amines in these lysine analogues interact with a diffuse column of charge in the pore that might be generated by the asymmetric positioning of the four D402 side chains. Such asymmetry has been suggested for the four glutamates at the homologous position in the calcium channel (Yang et al., 1993). Alternatively, the four D402 side chains may move in concert, depending on the position of the terminal amine at toxin position 27. A third possibility is that the shorter K27 analogues interact with channel residues other than D402.

Substitution of arginine and p-aminophenylalanine at position 27, significantly reduced toxin potency (Table 2). The guanido group in arginine and the aromatic group in p-aminophenylalanine, both positioned ~6.9–7.3 Å from

C<sub>α</sub>, may be too bulky (~4.2 Å, compared with ~1.7 Å for an amino group), to protrude into this narrowed part of the pore.

#### Estimated Dimensions of the Vestibule

Nine pairs of toxin–channel interactions at three channel positions have been identified (KTX-Kv1.3: R24–D386, R24–H404, F25–H404, R31–G380, L15–G380, K27–undetermined pore residue; ChTX-Kv1.3: R25–H404, W14–G380, K31–G380). Knowing the spatial relationships between these toxin residues, we have developed a topological map of the P-region. We have assumed that Kv1.3 forms a homotetramer with 4-fold symmetry and that toxin residue K27 projects into the center of the pore.

As illustrated by the schematic in Figure 7, our model places H404 (at the C-terminal end of the P-region) 4.5–7 Å from the central axis of the pore (or 9–14 Å from the H404 on the opposing subunit) based on the C<sub>α</sub> to C<sub>α</sub> distance between K27 and either R25 in ChTX (~4.5 Å) or F25 in KTX (~7 Å). Consistent with this picture, tetraethylammonium, a K<sup>+</sup> channel blocker that interacts with all four residues at this position (Kavanaugh et al., 1992), is ~9 Å wide, as is a hydrated K<sup>+</sup> ion (8–9 Å; Hille et al., 1993).

D386, at the N-terminal end of the P-region, is ~14–17 Å from the center of the pore, based on the distance from the C<sub>α</sub> of K27 and the farthest-reaching position of R24 in KTX; this would place D386 residues of opposing subunits 28–34 Å apart (Figure 7). D386 is 7–12 Å from H404, the lower limit being the distance between KTX-R24 and H404 (7–8 Å), and the upper limit being the sum of the distances between KTX-R24 and D386 (3–4 Å), and KTX-R24 and H404 (7–8 Å).

The outer mouth of the vestibule in the homotetramer is defined by the positions of the G380s in the tetramer. The distance between opposing G380 residues is estimated to be 28–32 Å (Figure 7) based on the distance between residues 14/15 and 31 in ChTX and KTX, corrected for the additional space of two Gln side chains (~4 Å per side chain difference between Q and G based on



Table 2. Effect of KTX-K27 Mutants on Kv1.3 Block

Residue at Position 27	Side Chain	Length (Å)	K <sub>d</sub>
Neutral amino acids			
Asparagine	CH <sub>2</sub> -C=O   NH <sub>2</sub>	3.6	64 ± 50
Norleucine	(CH <sub>2</sub> ) <sub>5</sub> -CH <sub>3</sub>	5.0	44 ± 13
Positively charged residues			
Diaminopropionate	CH <sub>2</sub> -NH <sub>3</sub> <sup>+</sup>	2.5	0.22 ± .13
Diaminobutyrate	(CH <sub>2</sub> ) <sub>2</sub> -NH <sub>3</sub> <sup>+</sup>	3.8	0.18 ± .11
Ornithine	(CH <sub>2</sub> ) <sub>5</sub> -NH <sub>3</sub> <sup>+</sup>	5.0	0.22 ± .08
Lysine (WT)	(CH <sub>2</sub> ) <sub>4</sub> -NH <sub>3</sub> <sup>+</sup>	6.3	0.15 ± .05
Thiohomolysine	CH <sub>2</sub> -S-(CH <sub>2</sub> ) <sub>5</sub> -NH <sub>3</sub> <sup>+</sup>	7.7	0.80 ± .50
Bulky positively charged residues			
Arginine	(CH <sub>2</sub> ) <sub>5</sub> -NH-C=NH   NH <sub>3</sub> <sup>+</sup>	7.3	2.0 ± .90
p-amino-phenylalanine	CH <sub>2</sub> -Ph-NH <sub>3</sub> <sup>+</sup>	6.9	>100

Numbers represent K<sub>d</sub> for channel block (nM) ± SD; n = 3–5. WT and mutant KTX peptides used in these experiments were synthesized (see Experimental Procedures). Note that this synthetic KTX is ~3-fold more potent in blocking Kv1.3 than commercial KTX (see Table 1).

data in Figure 6, where replacing G380 with Q converts a channel that is sensitive to KTX and ChTX to one that is resistant).

The vertical depth of the vestibule is estimated to be ~4–8 Å (Figure 7), based on the distance between the C<sub>α</sub> position of K31 in ChTX and a plane formed by the more distal carbon atoms of the side chains in R25 and M29, and the oxygen of Y36. The ion conduction pathway narrows to <4.2 Å at a distance of about 5–7 Å from the vestibule, based on the width of the terminal moieties in K27R and K27-p-aminophenylalanine (which block very poorly), and their distance from the toxin backbone (see Table 2).

### Developing a Model of the Kv1.3 Vestibule:

#### Docking Toxins

Using the estimated dimensions of the vestibule as constraints, we constructed a model of the Kv1.3 pore (modified from the *Shaker* model of Guy and Durrell, 1994) and have docked KTX and ChTX into the vestibule to identify new potential toxin–channel interactions and confirm the feasibility of experimentally determined ones (see Figures 3G and 3H).

#### KTX Docking

Docking of KTX was achieved by guiding K27 into the center of the channel pore, then rotating the toxin about the central pore axis until R24 was aligned with D386 (see Figure 3G). Consistent with our experimental data (see Figure 4), this configuration places F25 near H404. The three remaining H404s in the tetramer are close to toxin residues G10, M29, and T36. This docking configuration also places N30 and R31 close to D386 in the subunit opposite to that interacting with R24. In support of our model, R31 in AgTX2 has been experimentally demonstrated to be 3–4 Å from D431 in *Shaker*, the homologous residue to D386 (Hidalgo and MacKinnon, 1995). Also in keeping with this positioning, the N30D ChTX mutation abrogates the toxin's ability to block Kv1.3 (data not shown), possibly via electrostatic repulsion of D386. Simi-

lar results have been obtained with N30D and N30E ChTX mutants on the *Shaker* channel (Goldstein et al., 1994).

#### ChTX Docking

ChTX was docked into Kv1.3 by guiding K27 into the center of the pore, then rotating the toxin about the central axis until W14 and K31 projected toward G380 residues in opposing subunits (Figure 3H). This configuration places T8 adjacent to a third G380 in the homotetramer. Consistent with this picture, Goldstein et al. (1994) reported that T8 in ChTX is close to the *Shaker* residue homologous to G380, namely F425.

In summary, our Kv1.3 model is supported by considerable experimental data. The new interactions identified by

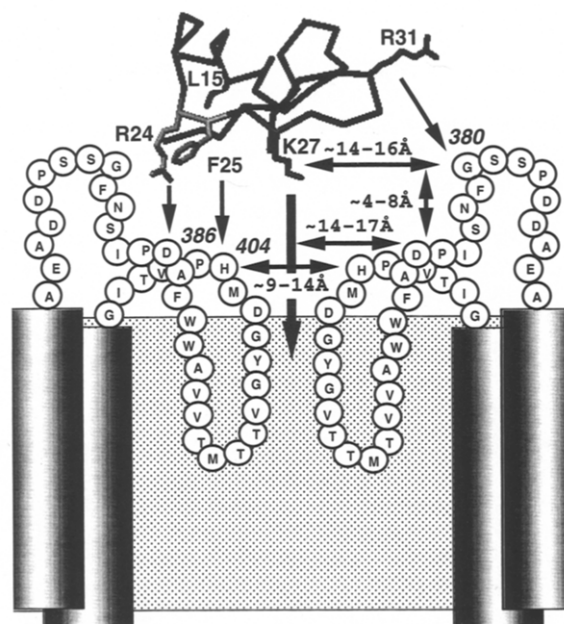


Figure 7. Schematic Model Showing the Sites of Interaction between KTX and the External Vestibule of Kv1.3

the docking experiments will guide further studies to map the vestibule.

### Discussion

The P-region forms a substantial part of the ion conduction pathway. We have used four scorpion toxins as structural probes, and analyzed nine toxin-channel interactions involving three channel positions; the data we have thus obtained support the existence of a shallow vestibule at the external entrance to the pore that is formed by residues within and around the P-region. Our topological map of this region places substantial spatial constraints on models of the P-regions of evolutionarily related ion channels.

We have compared our model of Kv1.3 with that of the *Shaker* vestibule, which has previously been mapped using ChTX and AgTX2 as molecular calipers. Our estimate of the width of the base of the Kv1.3 vestibule (28–34 Å) is consistent with a recent study that determined the base of the *Shaker* vestibule to be 22–30 Å wide (Hidalgo and MacKinnon, 1995). Based on the proximity of F425 in *Shaker* (homologous to G380 in Kv1.3) and T8/T9 in ChTX, the vertical depth of the *Shaker* vestibule was estimated to be about 12 Å, and the outer margin of the vestibule was suggested to lie ~13–15 Å radially from the central axis of the pore (Goldstein et al., 1994). The Kv1.3 vestibule is shallower (4–8 Å), but the width of the outer margin of the Kv1.3 vestibule, the distance between G380s in opposite subunits, is 28–32 Å, very similar to the *Shaker* estimate. We also determined three vestibular dimensions for which there are no existing estimates. The N- and C-terminal residues of the P-region (D386 and H404) and the center of the entrance to the pore form a triangle lying in the plane of the base of the vestibule; D386 is 7–12 Å from H404 and 14–17 Å from the central pore axis, whereas H404 is 4.5–7 Å from the center. The external entrance to the pore, limited by the four H404s in the tetramer, is 9–14 Å across. The ion conduction pathway narrows to 4–5 Å at a depth of 5–7 Å from the vestibule, although the precise residues that delineate this region remain undetermined. The values we report are consistent with the dimensions of the vestibule in the computational model of Kv2.1 proposed by Lipkind et al. (1995).

It is important to recognize that more or less subtle differences may exist among the topologies of the vestibules of Kv1.3 and related channels. For example, K427 in *Shaker* has been estimated to be ~5 Å from K11 in ChTX, and neutralization of this residue (K427N) greatly increases the channel's sensitivity to toxin block (Stocker and Miller, 1994). In contrast, placement of a positive charge at the homologous position in Kv1.3 (N382K) produces no appreciable change in sensitivity to toxin block (see Table 1), indicating that positively charged toxin residues are not in close proximity to channel residue 382. In a second example, the G380H mutation renders Kv1.3 resistant to KTX ( $K_d > 1000$  nM; see Table 1), whereas Kv1.1, which has a histidine at the homologous position, is effectively blocked by this toxin ( $K_d = 40$  nM; Grissmer et al., 1994). Lastly, the G380Q mutation makes Kv1.3 resistant to ChTX (see Figure 6), while the ChTX-sensitive

Kv1.2 ( $K_d = 14$  nM; Grissmer et al., 1994) has a glutamine at the homologous position (Chandy and Gutman, 1995).

Despite these differences, topological information about the Kv1.3 vestibule should aid in developing similar models for closely related voltage-gated and calcium-activated  $K^+$  channels, and possibly also the more distantly related voltage-dependent sodium and calcium channels. Such models could enhance our understanding of ion permeation and guide the development of novel, selective, and therapeutically useful ion channel modulating agents that bind in the channel vestibule. More specifically, it might now be possible to design new immunosuppressive agents that selectively block Kv1.3 in T-cells with the high affinity characteristic of toxin binding.

### Experimental Procedures

#### Generation of Toxin and Their Mutants

MgTX, KTX, and KTX-mutants were synthesized and folded using standard protocols (Fields et al., 1991; Garcia-Calvo et al., 1993; Bednarek et al., 1994), purified to homogeneity using reverse phase HPLC (Vydac C18 columns, water/acetonitrile gradient), and shown to exhibit the expected mass by electrospray mass spectrometry. The peptide content of HPLC eluants was measured by amino acid analysis (University of Michigan Protein and Carbohydrate Structure Facility, Ann Arbor, MI, and Harvard Microchemistry Facility, Cambridge, MA). Folded toxins were aliquoted and stored at  $-70^\circ\text{C}$ . A detailed protocol will be made available upon request from the authors (gchandy@uci.edu or gagutman@uci.edu). ChTX and KTX were also purchased from Peptides International (Louisville, KY); NTX was a gift from Robert Slaughter and Maria Garcia (Merck, Sharpe and Dohme, Rahway, NJ).

The ChTX-KTX loop chimera (ChTX residues 20–25 replaced with KTX residues 21–25) and the ChTX-W14S + K31G mutant were generated by recombinant methods (Park et al., 1991). A detailed protocol will be made available upon request (jaiyar@uci.edu). The ChTX mutants K31Q, K27N, and K27R were gifts from C. Miller, Brandeis University, Waltham, MA. All toxins were prepared in ND96 solutions (pH 7.6) containing 0.1% bovine serum albumin.

#### Nuclear Magnetic Resonance

All NMR experiments for KTX and MgTX were performed on 1.5–2.0 mM protein samples in 50 mM deuterated acetate buffer (pH 5.5) in 90%  $\text{H}_2\text{O}$ , 10%  $\text{D}_2\text{O}$  or 100%  $\text{D}_2\text{O}$ . Sequence-specific  $^1\text{H}$  assignments were obtained by total correlated spectroscopy (Braunschweiler and Ernst, 1983), NOE spectroscopy (Kumar et al., 1980), and DQF-COSY (Rance et al., 1983) techniques. Experiments were carried out on a Bruker AMX600 at  $15^\circ\text{C}$  and  $25^\circ\text{C}$ . Total correlated spectra were obtained using the DIPSI II spin locking sequence (Shaka et al., 1988) and a mixing time of 75 ms. NOE spectra were acquired at mixing times of 50, 100, 150, and 200 ms. Data processed on a Silicon Graphics Indigo using Felix Software (BIOSYM Technologies, San Diego, CA) were analyzed using EASY (Eccles et al., 1991). KTX and MgTX structures were calculated by distance geometry methods and refined by simulated annealing and conjugate gradient minimization techniques using DGI (BIOSYM Technologies) and an additional 100 steps of steepest descent and 200 steps of conjugate gradient energy minimization using the CFF91 force field in INSIGHTII (BIOSYM Technologies, San Diego, CA). Structures were subjected to an additional 200 steps of steepest descent and ~700 steps of conjugate gradient energy minimization using the AMBER force field in the Sander module in AMBER Version 4.0 (Pearlman et al., 1992). An ensemble of structures was created using the multiple structural overlap algorithm (Diamond, 1992).

#### KTX

The tertiary structure of KTX was determined with a total of 234 interproton distance restraints consisting of 16 intraresidue, 115 sequential, 17 ( $i, i + 2$ ), 12 ( $i, i + 3$ ), 4 ( $i, i + 4$ ), and 70 long-range NOEs obtained from NOE spectroscopy experiments at  $15^\circ\text{C}$  and  $25^\circ\text{C}$  and a mixing

time of 150 ms. Stereospecific assignments of  $\beta$ -methylene protons and the dihedral angle,  $\chi'$ , were obtained for 12 residues. Dihedral angle restraints for  $\phi$  were determined for 29 residues. Six H-bonding restraints were included based upon typical NOE patterns identified for the antiparallel  $\beta$  sheet. Disulfide bonds between C8–C28, C14–C33, and C18–C35 were included in the calculations as covalent bonds.

#### MgTX

The tertiary structure of MgTX was determined with a total of 293 interproton distance restraints consisting of 10 intraresidue, 140 sequential, 20 ( $i, i + 2$ ), 27 ( $i, i + 3$ ), 14 ( $i, i + 4$ ), and 92 long range NOEs (see discussion of KTX, above). Stereospecific assignments of  $\beta$ -methylene protons and  $\chi'$  were obtained for 7 residues, and dihedral angle restraints for  $\phi$  were determined for 30 residues. Four H-bonding restraints and disulfide bonds between C7–C29, C13–C34, and C17–C36 were included in the calculations as covalent bonds (see discussion above).

### Generation of Kv1.3 Mutants and Their Biophysical Characterization

#### Generating Mutants

Kv1.3 mutants were generated with a two-step PCR method (Ho et al., 1989). G380T, G380E, and G380Q were gifts from R. Swanson (Merck, Sharpe and Dohme, West Point, PA). cRNA was transcribed in vitro (Stratagene, La Jolla, CA) and injected into oocytes (*Xenopus laevis* purchased from NASCO, Fort Atkinson, WI) as described previously (Soreq and Seidman, 1992).  $K^+$  currents were measured at room temperature using the two-electrode voltage-clamp technique (Soreq and Seidman, 1992), and data were analyzed using pClamp software (version 5.5.1, Axon Instruments, Burlingame, CA). Whole oocytes were held at  $-100$  mV and depolarized to  $+40$  mV over 500 ms; time between pulses was 30 s. Capacitative and leak currents were subtracted prior to analysis using the P/4 procedure. The dissociation constant was calculated assuming a 1:1 binding of toxin to Kv1.3;  $K_d$  = concentration of toxin / ( $1/\text{fraction of unblocked current} - 1$ ) (Grissmer et al., 1990).

#### Electrostatic Compliance Measurement of Distance between D386 and R24

Electrostatic compliance, a measure of the strength of the charge–charge interaction between two specific residues, was calculated from the slopes of the two curves for a given set of toxin–channel mutants at 100 and 25 mM salt (Stocker and Miller, 1994). The theoretical form of the electrostatic compliance is given by:

$$\sigma(i,j) = \frac{\partial(\ln K_d)}{\partial q_{\text{chan}} \partial q_{\text{tox}}} = \frac{e^2 \exp(-r_{ij}/\lambda_D)}{kT4\pi\epsilon_0 D \gamma r_{ij}} \quad (1)$$

where  $r_{ij}$  is the separation between toxin and channel charges,  $e$  is electronic charge,  $k$  is the Boltzmann constant,  $\epsilon_0$  is permittivity of free space,  $D$  is the dielectric constant, and  $\gamma$  is a geometric factor that takes into account the electrostatics of the dielectric interface between water and protein (taken as 0.8). Separation between interacting charges was estimated by solving equation 1 for  $r_{ij}$  graphically.

We used a value of 80 for the dielectric constant for two reasons. First, bulk water parameters (Honig et al., 1993) were used to estimate distance between a residue deep in the *Shaker* vestibule (D431) and R24 in AgTX2 (Hidalgo and MacKinnon, 1995). Second, the vestibule has 4-fold symmetry and the toxin has no rotational symmetry. The toxin volume must therefore be considerably less than that of the vestibule, leaving room for water and electrolytes between toxin and channel. Thus, the relevant dielectric constant may be close to that of bulk water, even deep in the vestibule.

#### Electrostatic Compliance Measurement of Distance between H404:ChTX-R25 and KTX-R24

We generalized the electrostatic compliance method to include charge changes induced by pH titration. To obtain an experimental value of  $\sigma(i,j)$ , we calculated the change of  $\ln K_d$  for a given change in channel charge, for both ChTX and ChTX-R25D. We assume that the partial charge on Kv1.3's H404 residue is described by equation 2:

$$q_{\text{hs}} = \frac{K_d[\text{H}^+]}{1 + K_d[\text{H}^+]} \quad (2)$$

where  $K_d$  is the dissociation constant, and  $[\text{H}^+]$  is the proton concentration. The derivative of pH with respect to charge,  $1/q_{\text{hs}} \ln(10)$ , was multiplied by the least square slopes,  $\partial \ln K_d / \partial \text{pH}$  (obtained experimentally), to give the term  $\partial(\ln K_d) / \partial q_{\text{hs}}$ , where  $q_{\text{hs}}$  is the partial charge on the histidine (in units of electronic charge) and varies from 0 to +1. The  $\sigma(i,j)$  value was then determined by subtracting the slope of the WT toxin from that of its mutant (ChTX-R25D or KTX-R24D) and dividing the value by 2 (absolute change in charge on the toxin). For these calculations, we assumed the dielectric constant to be 80 and a pK for the histidine of 6.2 (also see Creighton, 1984). We calculated the value of  $\partial \text{pH} / \partial q_{\text{hs}}$  at pH 6.4, the midpoint of our experimental curve (see Results).

#### Thermodynamic Mutant Cycle Analysis

Hidalgo and MacKinnon (1995) defined  $\Omega$  as a measure of the interaction between charged residues — a value of 1 representing no coupling and values different from 1 indicating progressively stronger interactions:

$$\Omega = \frac{K_d[\text{WT toxin:WT Kv1.3}] \times K_d[\text{mut toxin:mut Kv1.3}]}{K_d[\text{mut Kv1.3:WT toxin}] \times K_d[\text{WT Kv1.3:mut toxin}]} \quad (3)$$

For the R25:H404 and R24:H404 interactions, WT and mutant Kv1.3  $K_d$ s were measured at pH 6.8 and 6.0.

The difference in free energy of an interaction between specific residues in WT/WT versus mutant/mutant interactions is given by equation 4, which converts values into coupling energies:

$$RT \ln \Omega = RT \ln \left( \frac{K_{\text{dwt}}}{K_{\text{dmt}}} \right) = E \quad (4)$$

Assuming bulk water parameters and using Debye–Huckel theory, we used coupling energies to estimate charge–pair separation by solving the following equation for  $r$ :

$$\partial(r, q_1, q_2, \lambda_D) = \frac{q_1 q_2 e^2 \exp(-r/\lambda_D)}{4\pi\epsilon_0 D \gamma r} \quad (5)$$

where  $q_1$  is the change in charge on the channel between mutant and WT,  $q_2$  is the change in charge on the toxin between mutant and WT,  $D$  is the dielectric constant (taken as 80),  $\epsilon_0$  is the permittivity of free space,  $\gamma$  is a distance-dependent geometrical factor described above (taken as 0.8), and  $\lambda_D$  is the Debye length.

### Modeling Structures

#### Modeling NTX

To create a model of NTX, we used our experimentally determined structure for MgTX and made the following substitutions: L14S, P15K, A19E, Q20L, F21Y, Q23S, P38N, and H39N. The resulting model of NTX was minimized in SYBYL 6.1 (Tripos Inc., St. Louis, MO) using Kollman force field and charges.

#### Modeling the Kv1.3 Pore

To create a model of the Kv1.3 pore, F425, K427, T449, G452, F453, and W454 in the model of the *Shaker* channel (Guy and Durell, 1994) were mutated to G380, N382, H404, T407, I408, and G409, respectively. Assuming perfect 4-fold symmetry, the distances we experimentally estimated between residues G380, D386, and H404 (see Results) were included as constraints during minimization of the channel with SYBYL.

### Acknowledgments

This work was supported by grants from the National Institutes of Health (AI24783; K. G. C.) and Pfizer, Inc. (Groton; K. G. C. and G. A. G.), and by an American Heart Association Fellowship (J. A.). We thank H. R. Guy (NIH, MD) for supplying us with models of the *Shaker*  $K^+$  channel; J. Stroh (Pfizer Inc., CT) for support in characterizing KTX; and M. Cahalan (UCI, CA), S. Grissmer (Univ. Ulm), S. Alpers (Harvard Univ., MA), C. Miller (Brandeis Univ., MA), and G. Ehring (UCI, CA) for helpful discussions.

The costs of publication of this article were defrayed in part by the payment of page charges. This article must therefore be hereby

marked "advertisement" in accordance with 18 USC Section 1734 solely to indicate this fact.

Received June 23, 1995; revised July 25, 1995.

## References

- Bednarek, M.A., Bugianesi, R.M., Leonard, R.J., and Felix J.P. (1994). Chemical synthesis and structure-function studies of margatoxin, a potent inhibitor of a voltage-dependent potassium channel in human T lymphocytes. *Biochem. Biophys. Res. Commun.* **198**, 619-625.
- Bontems, F., Gilquin, B., Roumestand, C., Menez, A., and Toma, F. (1992). Analysis of side-chain organization of a refined model of charybdotoxin: structural and functional implications. *Biochem.* **31**, 7756-7764.
- Braunschweiler, L., and Ernst, R.R. (1983). Coherence transfer by isotropic mixing: application to proton spectroscopy. *J. Magn. Reson.* **53**, 521-528.
- Burley, S.K., and Petsko, G.A. (1985). Aromatic-aromatic interactions: a mechanism of protein structure stabilization. *Science* **229**, 23-28.
- Burley, S.K., and Petsko, G.A. (1989). Electrostatic interactions in aromatic oligopeptides contribute to protein stability. *Trends Biotech.* **7**, 354-359.
- Chandy, K.G., and Gutman, G.A. (1995). Voltage-gated K<sup>+</sup> channel genes. In *Handbook of Receptors and Channels: Ligand and Voltage-Gated Ion Channels*, A. North, ed. (Boca Raton, FL: CRC Press), pp. 1-71.
- Creighton, T.E. (1984). *Proteins: Structures and Molecular Principles* (New York: W.H. Freeman and Co.).
- DeCoursey T.E., Chandy, K.G., Gupta, S., and Cahalan, M.D. (1984). Voltage-gated potassium channels in human T lymphocytes: a role in mitogenesis? *Nature* **307**, 465-467.
- Diamond, R. (1992). On the multiple simultaneous superposition of molecular structures by rigid body transformations. *Prot. Sci.* **1**, 1279-1287.
- Eccles, C., Guntert, P., Billeteri, M., and Wuthrich, K. (1991). Efficient analysis of protein 2D NMR spectra using the software package EASY. *J. Biomol. NMR* **1**, 111-130.
- Fernandez, I., Romi, R., Szendeffy, S., Martin-Eauclaire, M.F., Rochat, H., Van Rietschoten, J., Pons, M., and Giralt, E. (1994). Kaliotoxin (1-37) shows structural differences with related potassium channel blockers. *Biochem.* **33**, 14256-14263.
- Fields, C.G., Lloyd, D.H., Macdonald, R.L., Otteson, K.M., and Noble, R.L. (1991). HBTU activation for automated Fmoc-solid phase toxin synthesis. *Pept. Res.* **4**, 95-101.
- Garcia-Calvo, M., Leonard, R.J., Novick, J., Stevens, S.P., Schmalhofer, W., Kaczorowski, G.J., and Garcia, M.L. (1993). Purification, characterization, and biosynthesis of margatoxin, a component of *Centruroides margaritatus* venom that selectively inhibits voltage-dependent potassium channels. *J. Biol. Chem.* **268**, 18866-18874.
- Goldstein, S.A.N., and Miller, C. (1993). Mechanism of charybdotoxin block of a voltage-gated K<sup>+</sup> channel. *Biophys. J.* **65**, 1613-1619.
- Goldstein, S.A.N., Pheasant, D.J., and Miller, C. (1994). The charybdotoxin receptor of a *Shaker* K<sup>+</sup> channel: peptide and channel residues mediating molecular recognition. *Neuron* **12**, 1377-1388.
- Grissmer, S., Dethlefs, B., Wasmuth, J.J., Goldin, A.L., Gutman, G.A., Cahalan, M.D., and Chandy, K.G. (1990). Expression and chromosomal localization of a lymphocyte K<sup>+</sup> channel gene. *Proc. Natl. Acad. Sci. USA* **87**, 9411-9415.
- Grissmer, S., Nguyen, A.N., Aiyar, J., Hanson, D.C., Mather, R.J., Gutman, G.A., Karmilowicz, M.J., Auperin, D.D., and Chandy, K.G. (1994). Pharmacological characterization of five cloned voltage-gated K<sup>+</sup> channels, types Kv1.1, 1.2, 1.3, 1.5 and 3.1, stably expressed in mammalian cell lines. *Molec. Pharmacol.* **45**, 1227-1234.
- Guy, H.R., and Durell, S.R. (1994). Using sequence homology to analyze the structure and function of voltage-gated ion channel proteins. In *Molecular Evolution of Physiological Processes*, Douglas M. Farmbrough, ed. (New York: Rockefeller University Press), pp. 197-212.
- Hidalgo, P., and MacKinnon, R. (1995). Revealing the architecture of a K<sup>+</sup> channel pore through mutant cycles with a peptide inhibitor. *Science* **268**, 307-310.
- Hille, B. (1993). Elementary properties of ions in solution. In *Ionic Channels of Excitable Membranes*, 2nd Edition (Massachusetts: Sinauer Associates), pp. 261-290.
- Ho, S.N., Hunt, H.D., Horton, R.M., Pullen, J.K., and Pearse, L.R. (1989). Site-directed mutagenesis by overlap extension using the polymerase chain reaction. *Gene* **77**, 51-59.
- Honig, B., Sharp, K., and Yang, A.S. (1993). Macroscopic models of aqueous solutions—biological and chemical applications. *J. Phys. Chem.* **97**, 1101-1109.
- Johnson, B.A., and Sugg, E.E. (1992). Determination of the three-dimensional structure of iberiotoxin in solution by <sup>1</sup>H nuclear magnetic resonance spectroscopy. *Biochem.* **31**, 8151-8159.
- Johnson, B.A., Stevens, S.P., and Williamson, J.M. (1994). Determination of the three-dimensional structure of margatoxin by <sup>1</sup>H, <sup>13</sup>C, <sup>15</sup>N triple resonance nuclear magnetic resonance spectroscopy. *Biochem.* **33**, 15061-15070.
- Kavanaugh, M.P., Hurst, R.S., Yakel, J., Varnum, M.D., Adelman, J.P., and North, R.A. (1992). Multiple subunits of a voltage-dependent potassium channel contribute to the binding site for tetraethylammonium. *Neuron* **8**, 493-497.
- Krezel, A.M., Kasibhatla, C., Hidalgo, B., MacKinnon, R., Wagner, G. (1995). Solution structure of the potassium channel inhibitor, Agitoxin 2: caliper for probing channel geometry. *Prot. Sci.* **4**, 1478-1489.
- Kumar, A., Ernst, R.R., and Wüthrich, K. (1980). A two-dimensional nuclear Overhauser enhancement (2D-NOE) experiment for the elucidation of complete proton-proton cross-relaxation networks in biological molecules. *Biochem. Biophys. Res. Commun.* **95**, 1-6.
- Leonard, R.J., Garcia, M.L., Slaughter, R.S., and Reuben, J.P. (1992). Selective blockers of voltage-gated K<sup>+</sup> channels depolarize human T lymphocytes: mechanism of the antiproliferative effect of charybdotoxin. *Proc. Natl. Acad. Sci. USA* **89**, 10094-10098.
- Lewis, R.S., and Cahalan, M.D. (1995). Potassium and calcium channels in lymphocytes. *Annu. Rev. Immunol.* **13**, 623-654.
- Lin, C.S., Boltz, R.C., Blake, J.T., Nguyen, M., Talento, A., Fischer, P.A., Springer, M.S., Sigal, N.H., Slaughter, R.S., Garcia, M.L., et al. (1993). Voltage-gated K<sup>+</sup> channels regulate calcium-dependent pathways involved in human T lymphocyte activation. *J. Exp. Med.* **177**, 637-645.
- Lipkind, G.M., Hanck, D.A., and Fozzard, H.A. (1995) A structural motif for the voltage-gated potassium channel pore. *Proc. Natl. Acad. Sci. USA* **92**, 9215-9219.
- MacKinnon, R., and Miller, C. (1988). Mechanism of charybdotoxin block of Ca<sup>2+</sup>-activated K<sup>+</sup> channels. *J. Gen. Physiol.* **91**, 335-349.
- MacKinnon, R., Heginbotham, L., and Abramson, T. (1990). Mapping the receptor site for charybdotoxin, a pore-blocking potassium channel inhibitor. *Neuron* **5**, 767-771.
- Park, C.-S., and Miller, C. (1992). Interaction of charybdotoxin with permeant ions inside the pore of a K<sup>+</sup> channel. *Neuron* **9**, 307-313.
- Park, C.-S., Hausdorff, S.F., and Miller, C. (1991). Design, synthesis and functional expression of a gene for charybdotoxin, a toxin blocker of K<sup>+</sup> channels. *Proc. Natl. Acad. Sci. USA* **88**, 2046-2050.
- Pearlman, D.A., Case, D.A., Caldwell, J.C., Seibel, G.L., Singh, C., Weiner, P., and Kollman, P.A. (1991). AMBER 4.0 Program (San Francisco: University of California).
- Price, M., Lee, S.C., and Deutsch, C. (1989). Charybdotoxin inhibits proliferation and interleukin 2 production in human peripheral blood lymphocytes. *Proc. Natl. Acad. Sci. USA* **86**, 10171-10175.
- Rance, M., Sorensen, O.W., Bodenhausen, G., Wagner, G., Ernst, R.R. (1983). Improved spectral resolution in COSY <sup>1</sup>H-NMR spectra of proteins via double quantum filtering. *Biochem. Biophys. Res. Commun.* **117**, 479-485.
- Shaka, A.J., Lee, C.J., and Pines, A. (1988). Iterative schemes for bilinear operators. Application to spin decoupling. *J. Magn. Reson.* **77**, 274-293.

Soreq, H., and Seidman, S. (1992). *Xenopus* oocyte microinjection from gene to protein. *Meth. Enzymol.* 207, 225–265.

Stampe, P., Kolmakova-Partensky, L., and Miller, C. (1994). Intimations of K<sup>+</sup> channel structure from a complete functional map of the molecular surface of charybdotoxin. *Biochem.* 33, 443–540.

Stocker, M., and Miller, C. (1994). Electrostatic distance geometry in a K<sup>+</sup> channel vestibule. *Proc. Natl. Acad. Sci. USA.* 91, 9509–9513.

Würthrich, K. (1986). *NMR of Protein and Nucleic Acids* (New York: John Wiley & Sons).

Yang, J., Ellinor, P.T., Sather, W.A., Zhang, J.-F., and Tsien, R.W. (1993). Molecular determinants of Ca<sup>2+</sup> selectivity and ion permeation in L-type Ca<sup>2+</sup> channels. *Nature* 366, 158–161.